JOURNAL OF MATERIALS SCIENCE **36** (2001) 4059–4069

# Fabrication of in situ TiC reinforced aluminum matrix composites

X. C. TONG, A. K. GHOSH
*Department of Materials Science and Engineering, The University of Michigan, Ann Arbor, Michigan 48109-2136, USA*
*E-mail: xtong@engin.umich.edu*

In the present work, the room and elevated temperature mechanical behavior of Al/TiC, high-strength Al-Si/TiC and the elevated temperature-resistant Al-Fe(-V-Si)/TiC composites has been evaluated. The microstructural characteristics of ingot metallurgy (IM) or rapid solidification (RS) Al-Si/TiC and Al-Fe(-V-Si)/TiC composites could be thought of as a combination of the related alloy matrix microstructures and the IM or RS Al/TiC composites. The IM Al/TiC and the Al-Si/TiC composites show superior strength and ductility to the relevant aluminum based composites.The RS Al/TiC and the Al-Fe-V-Si/TiC exhibit high Young's moduli and substantial improvements in room and elevated temperature tensile properties compared to those of rapidly solidified alloys and conventional composites.The Young's modulus values of RS Al/TiC and Al-Fe-V-Si/TiC composites are well within Hashin-Shtrikman limits in keeping with the strong interfacial bonding. In the micromechanics approach, the principal strengthening mechanisms for the present dispersed particle-hardened RS in situ Al-TiC composites would include Orowan strengthening, grain-size and substructure strengthening, and solid-solution strengthening. The RS technique was used in the present work to maximize strength and ductility for a particular volume fraction, and influence the degree of flexibility available to meet these requirements: a fine, uniform particle size distribution; a high interfacial strength; control of particle shape; and a ductile matrix. 

## 1. Introduction

Metal matrices reinforced with ceramic particles have been developed in recent years for various automobile and other structural applications. Different particles such as SiC, $Al_2O_3$, $TiB_2$, $B_4C$, TiC [1–5] have been recognized as potential reinforcements for metal, as the dispersion of these particles enhances the elastic modulus, hardness, tensile strength at room and elevated temperatures and wear resistance of the alloys. The particle reinforced composites are conventionally prepared either by powder technology or liquid metallurgy, where the ceramic particles are directly incorporated into solid or liquid matrices respectively. However, metal matrices reinforced with ceramic particles formed in situ are an emerging group of discontinuously reinforced composites, that have distinct advantages over the conventional composites [6, 7]. Both liquid phase and solid phase processes are being studied to produce in situ particle composites based on metal matrices. In liquid phase processes, solid , liquid or gaseous phases are introduced into a liquid metal/alloy to react with the base metal or its alloying elements and hence to produce reinforcement phases. In solid phase processes, elements or elements/compounds are blended, compacted and heated at a selected temperature to form the desired reinforcements. Both techniques produce very fine reinforcements in the matrices. The interfaces are clean and are semicoherent in some cases. Mechanical properties of in situ composites are comparable with or better than those of conventional composites [7].

In the present work, we highlight a novel in situ process in which traditional ingot metallurgy (IM) plus rapid solidification (RS) techniques are used to produce Al-TiC composites with refined microstructures and enhanced dispersion hardening of the reinforcing phases. In Part I of this investigation [8], the microstructural evolution of the in situ Al-TiC composites has been examined. The purpose of the present study is to access/exploit the high-strength type Al-Si/TiC composites and the elevated temperature-resistance type Al-Fe(-V-Si)/TiC composites based on the preparation of the in situ Al-TiC composites. In particular, the room and elevated temperature mechanical behavior has been evaluated.

## 2. Experimental procedure

The materials and related parameters used in this study are summarized in Table I. Details of material preparation procedure and the chemical composition as well as microstructural characterization studies are given in Part I of this investigation [8]. In Table I, the ribbons of RA20* and RAF2* were milled into powder

TABLE I Typical materials and processing parameters used

| Number IM RS | Composition (Wt. Pct.) | RS parameters Tempt (K) | $t_{hold}$ (min) | $d_{ribbon}$ ($\mu$m) |
|---|---|---|---|---|
| IA10 RA10 | Al-4Ti-0.65C | 1623 | 5 | 70-80 |
| IA11 RA11 | Al-7Ti-0.65C | 1623 | 5 | 70-80 |
| IA20 RA20 | Al-5Ti-1.0C | 1623 | 5 | 70-80 |
| RA20* | Al-5Ti-1.0C | 1623 | 0 | 70-80* |
| IA30 RA30 | Al-6Ti-2.0C | 1623 | 5 | 70-80 |
| IAF1 RAF1 | Al-6Fe/5Ti-1.0C | 1623 | 0 | 70-80 |
| IAF2 RAF2 | Al-6.5Fe-0.6V-1.3Si/5Ti-1.0C | 1523 | 0 | 80-90 |
| RAF2* | Al-6.5Fe-0.6V-1.3Si/5Ti-1.0C | 1623 | 0 | 40-50* |
| IAS0 RAS0 | Al-10Si/5Ti-1.0C | 1473 | 0 | 80-90 |

*The ribbons were milled into powder which was subsequently canned and extruded to 12.0 mm diameter.

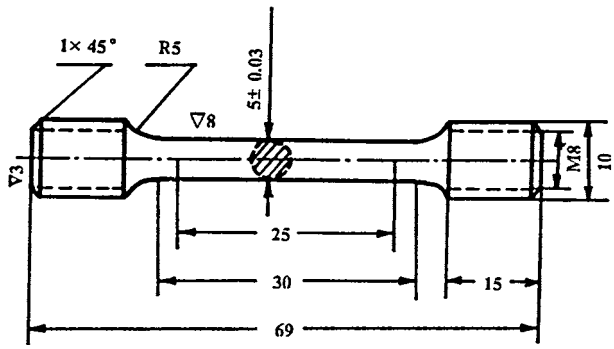


*Figure 1* Schematic tensile specimen.

(about 250 and 100 $\mu$m respectively) which was subsequently canned and treated in vacuum (about $10^{-5}$ Torr) at 573 K for 1 h in order to remove the hydrate layer from the Al surface, then extruded at 673 K with a 16:1 extrusion ratio to 12.0 mm diameter.

Room temperature tensile tests were carried out on as cast (IA10, IA11, IA20, IA30, IAF1, IAF2, IAS0) and RS extruded (RA20* and RAF2*) samples, and the RS extruded samples (RA20* and RAF2*) were selected to do elevated temperature tension tests. The tensile specimen size was given in Fig. 1. Tensile tests were conducted using an Instron 8032 testing machine. The strain rate was $10^{-3}$ per second. The elevated temperature tension tests were carried out in an electrical resistance furnace with a temperature accuracy of $\pm 3$ K. Before testing under a tensile load the samples were allowed to equilibrate at temperature for half an hour. The tensile fracture surfaces were investigated using a JEOL JSM-35C scanning electron microscope (SEM).

The elastic moduli of the extruded RA20* and RAF2* samples (0.009 m diameter and 0.2 m length) were measured using a resonance technique. This technique analyzes the vibrational behavior of the samples following an impulse excitation [9].

## 3. Results

### 3.1. Microstructures

Microstructures of IA10, IA20, IA30 and RA10, RA20, RA30 (Table I) have been characterized in the Part I [8], whereas the microstructural characteristics of the IAF1, IAF2, IAS0, RAF2 and RAS0, as shown in Figs 2

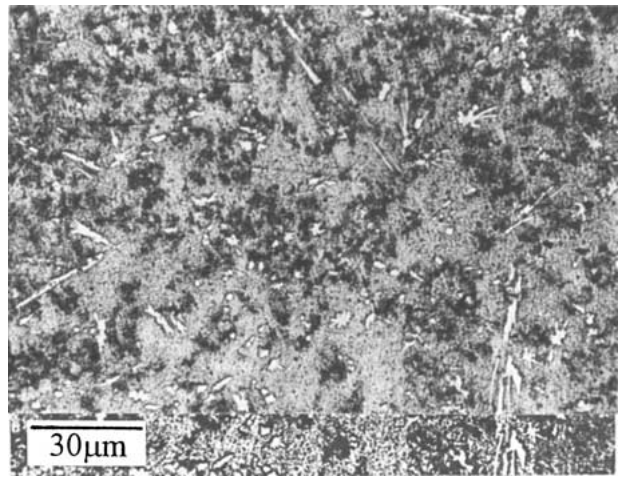


(a)

(b)

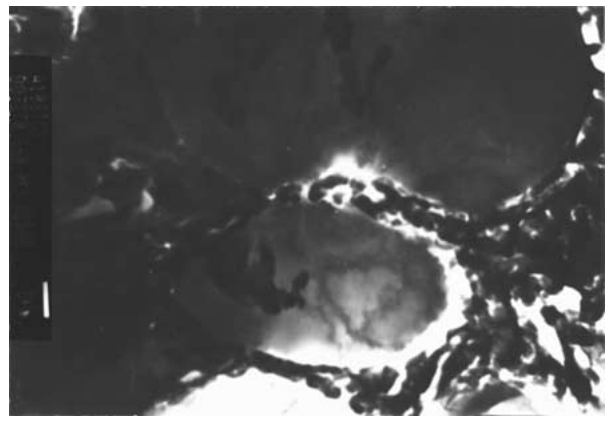

(c)

*Figure 2* As-cast microstructures of IM in situ composites of IAF1 (a), IAF2 (b) and IAS0 (c).

and 3, can be thought as a combination of the related alloy matrix microstructures and those of the IA20 or RA20 . However, Figs 4 and 5 shown that the extruded microstructures of RA20* and RAF2* were similar to those of RA20 and RAF2, respectively.

### 3.2. Mechanical behavior

#### *3.2.1. IM in situ composites*

The ambient temperature engineering stress-strain curves for the IA10 to 30, IAF1 to 2 and IAS0 are shown in Fig. 6. The results of the ambient temperature tensile testing on these IM in situ composites are summarized in Table II and compared to those of equivalent materials prepared by XD and casting routes.

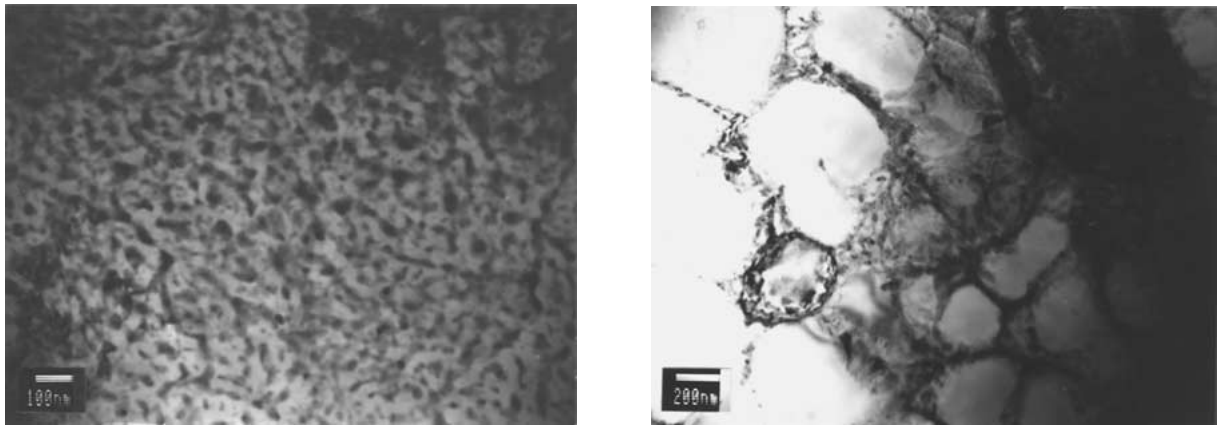


(a) (b)

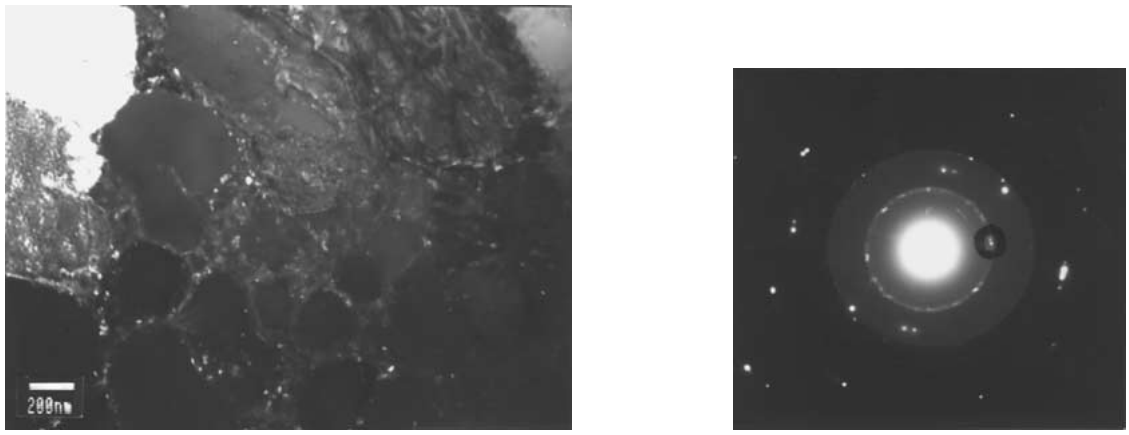


(c) (d)

*Figure 3* Rapidly solidified microstructures of RS in situ composites of RAF2 (a) and RAS0 : BF (b), DF (c) and related SAED pattern (d).

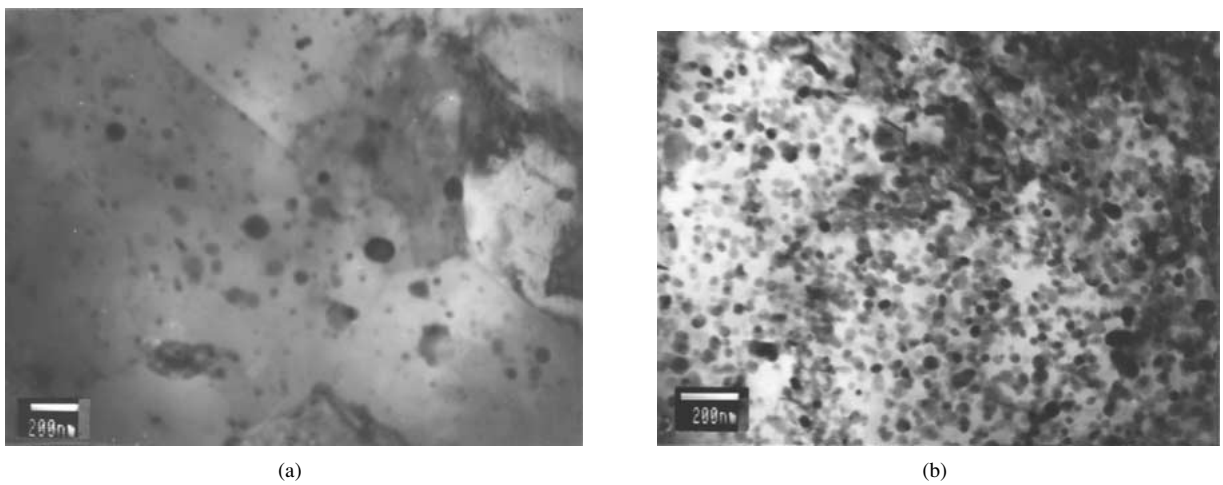


(a) (b)

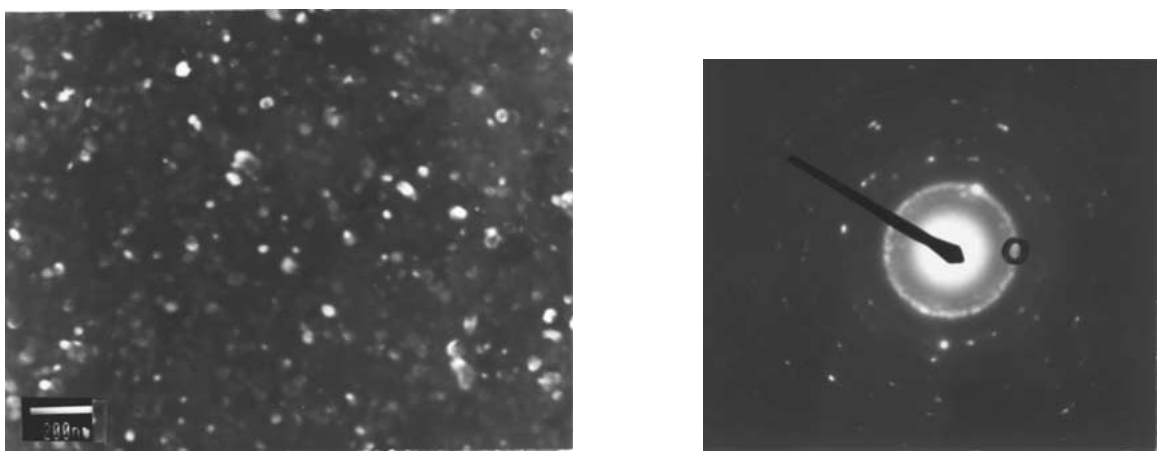


(c) (d)

*Figure 4* Microstructures of RS extruded in situ composites of RA20* (a) and RAF2* : BF (b), DF (c) and related SAED pattern (d).

TABLE II Tensile properties of the IM in situ composites

| Material | $\sigma_{UTS}$ (MPa) | $\sigma_{YS}$ (MPa) | El (Pct) | $\varphi$ (Pct) | Reference |
|---|---|---|---|---|---|
| IA10 | 206 | 144 | 21.1 | 31.3 | |
| IA11 | 211 | 141 | 23.3 | 41.8 | |
| IA20 | 242 | 169 | 20.0 | 38.4 | Present |
| IA30 | 168 | 130 | 16.7 | 28.4 | work |
| IAF1 | 218 | 165 | 7.3 | 5.6 | |
| IAF2 | 159 | 160 | 4.4 | 3.3 | |
| IAS0 | 369 | 242 | 8.1 | 7.6 | |
| Al-7Si-Mg-Be (die casting) | | | | | Ref. [10] |
| 15 vol.%SiC | 195 | 127 | 1.5 | | |
| 20 vol.%SiC | 216 | 148 | 1.3 | | |
| Al-15 vol.%TiC ($0.7\ \mu$m) | | | | | Ref. [11] |
| XD + extrusion | 154 | 110 | 20.0 | | |
| Annearing (913 K, 96h) | 210 | 152 | 2.3 | | |

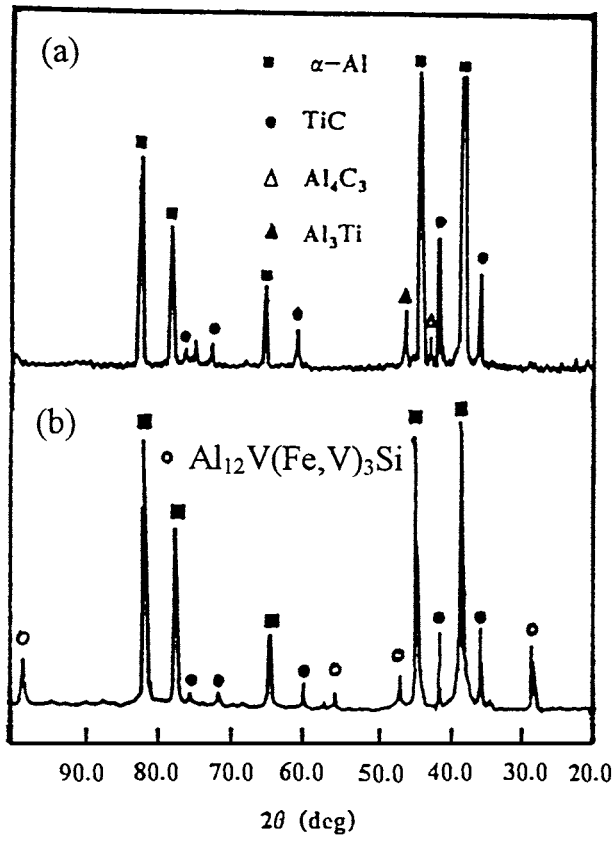


*Figure 5* X-ray diffraction patterns of RS extruded in situ composites of RA20* (a) and RAF2* (b).

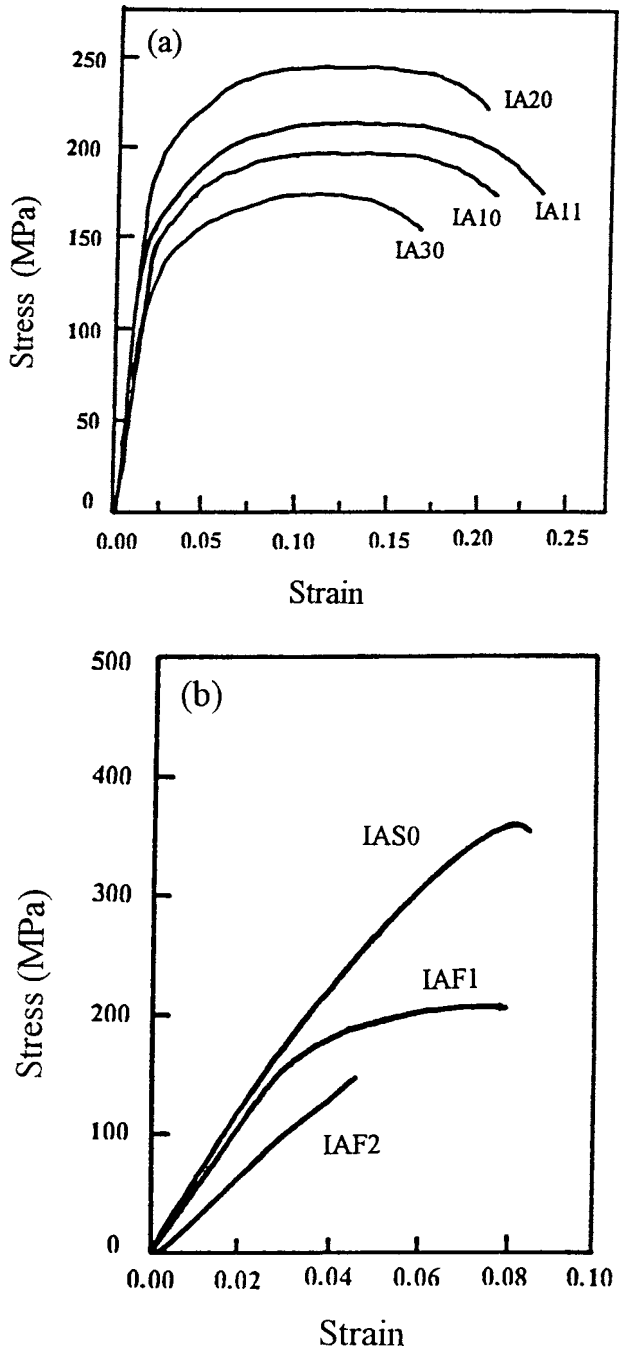


*Figure 6* Ambient temperature engineering stress-strain curves of the IM in situ composites of IA10-30 (a), IAF1-2, and IAS0 (b). The decrease in elongation to failure can be clearly seen.

Except for IA30, the IM in situ Al-TiC composites, IA10, IA11, especially IA20 possess superior combination of tensile strength and percentage elongation, to the relevant aluminum based composites [10, 11]. Fig. 7a–d show the fracture surface of tensile samples of the IM Al-TiC composites. The presence of dimples on the fracture surface indicate a ductile mode of fracture for the IA10, IA11 and IA20; the fracture surface of IA 30 emerges the grain crack probably results from the needle-like brittle $Al_4C_3$ phase particles by interconnection of the cracked $Al_4C_3$ particles through micro void coalescence (MVC) of matrix ligaments, and results in its inferior tensile strength and toughness. Moreover, careful examination of all of the samples revealed the presence of TiC inside some of the dimples, indicating the interfacial debonding is the important factor causing the failure of the materials. However, because the interface should be strong (clean) and the reinforcement particles are also strong with few defects, the fracture occurs by MVC of matrix alone since the matrix is having very low shear strength, therefore, it should be thought that the IA10, IA11 and IA20 composites fail by shear of the matrix. In the light of this statement, strengthening the matrix itself improve composite properties. The annealed sample of Al-15vol.%TiC, for instance, has a higher strength than its as-extruded one [11], the reason being that the annealing strengthens the matrix.

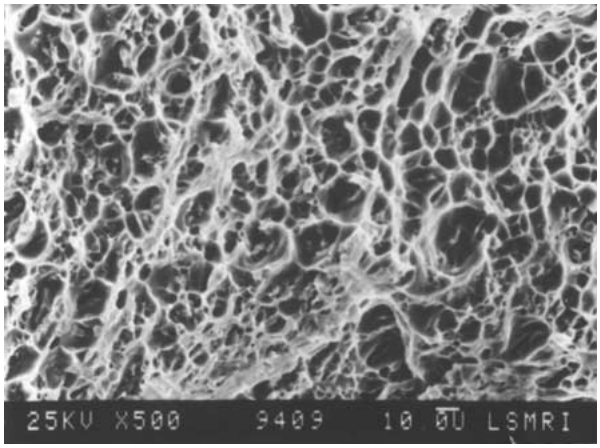


(a)

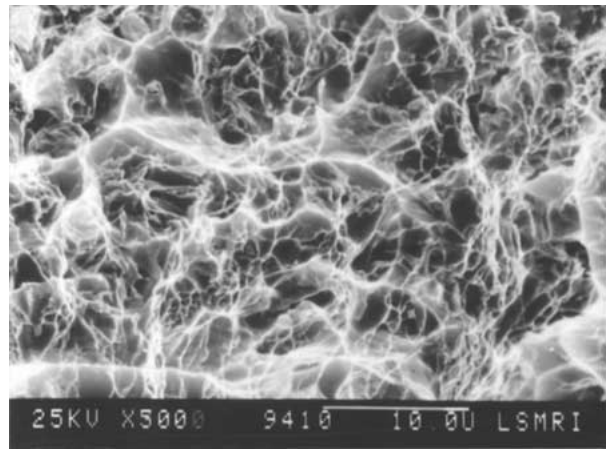


(b)

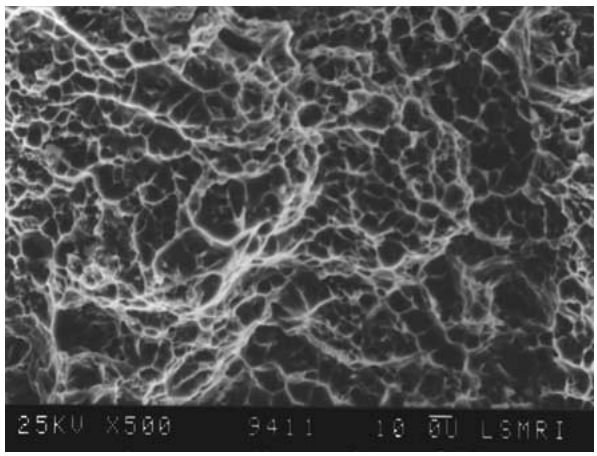


(c)

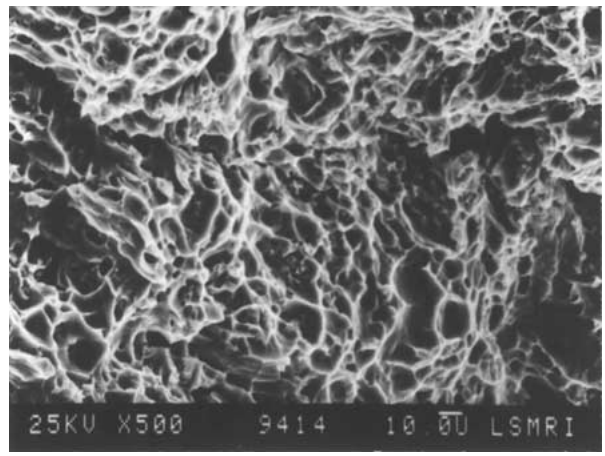


(d)

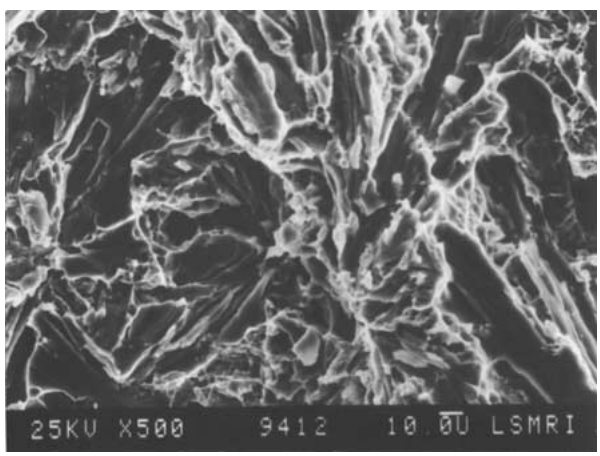


(e)

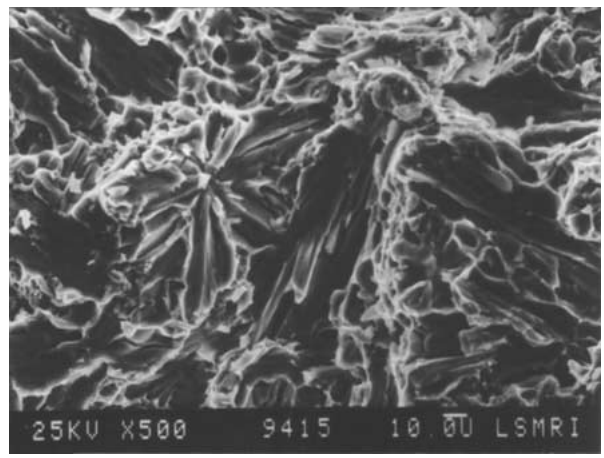


(f)

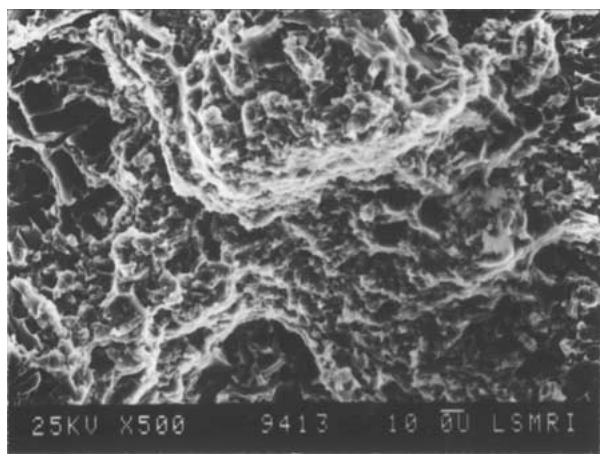


(g)

*Figure 7* Tensile fracture surfaces of IM in situ composites: IA10 (a), IA11 (b), IA20 (c), IA30 (d), IAF1 (e), IAF2 (f), IAS0 (g); SEM images.

Consequently, in the present work the Al-Si/TiC(IAS0) and Al-Fe/TiC(IAF1, 2) were designed and examined. However, the tensile properties of IAF1 and IAF2 were poor since large intermetallic compounds were formed in the ingot casting. Fig. 7e–g show that the intermetallic inclusions fractured by a cleavage mechanism, whereas the remaining composite fractured by a quasicrystalline mechanism [12]. Comparatively, the IAS0 shows reletive high strength and good toughness, which could match with those of 356/15vol.%SiCp(T61) and 380/20 vol.% Cp(F) [13]. Fractgraphs of the IAS0 indicates a quasi-ductile fracture. Microstructural refining of this sort of composite, however, would largely improve their properties, as shown in the following.

### *3.2.2. RS extruded in situ composites*

Young's moduli for the RS in situ composites RA20* and RAF2* at room temperature were tested as 81 GPa and 91 GPa.

Representative engineering stress/strain curves obtained for RA20* and RAF2* at various temperatures from 298 K and 673 K (Fig. 8) all exhibit well-defined yielding. Values of yield strength and the corresponding ultimate strength and ductility data of RA20* and RAF2* as a function of temperature are summarized in Table III. The tensile properties tend to decrease normally with an increasing test temperature. The room and elevated temperature properties of RA20* compare favorably to those of the materials shown in Ref. [13]. Fig. 9a–d show the tensile fracture surfaces of the composite samples. The fractgraphs reveal a typical ductile fracture surface for 298 K and 573 K, and the grain crack on fracture surface for 623 K and 673 K.

Moreover, the test results shown in Table III indicate that the room and elevated temperature strength of RAF2* compare favorably to those of the FVS0611 (with composition close to the matrix of RAF2*), are superior to those of FVS0812, but are slightly inferior to those of FVS1212. However, the ductility of RAF2* are slightly lower than those of FVS0611, close to FVS0812, and super to FVS1212 [14]. The fracture surface characteristics of RAF2* are similar to those of RA20*, as shown in Fig. 9e–h.

## 4. Discussion

### 4.1. Modulus measurements

Following analysis similar to that of Ref. [15], the lower and upper bound values of Young's modulus $E$ can be estimated from the H-S relationship (Assuming elastic isotropy quasihomogeneous solid, Hashin and Shtrikman used a variational technique based on linear elastic theory to calculate the upper and lower bound values of the elastic constants for two phase materials):

$$E = 9KG/(3K + G) \quad (1)$$

where $K$ is the bulk modulus, and $G$ is the shear modulus. A chemical bonded interface will give an $E$ value

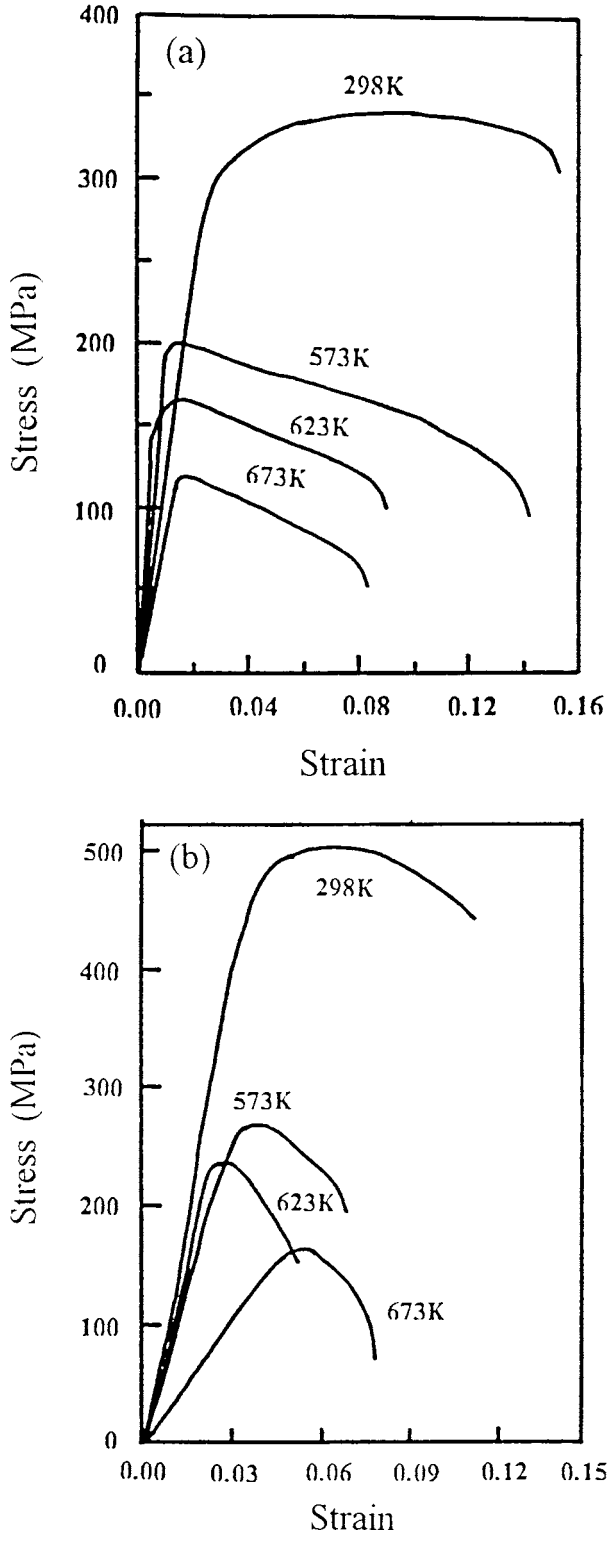


*Figure 8* Engineering stress-strain plots for RS extruded in situ composites of RA20* (a) and RAF2* (b) at different temperatures (298 to 673 K).

TABLE III Elevated temperature mechanical properties of RA20* and RAF2*

| Material | Temperature (K) | $\sigma_{UTS}$ (MPa) | $\sigma_{YS}$ (MPa) | El (Pct) | $\varphi$ (Pct) | E (GPa) |
|---|---|---|---|---|---|---|
| RA20* | 298 | 336.1 | 296.3 | 14.9 | 24.5 | 81 |
| | 573 | 198.6 | 191.5 | 14.4 | 27.0 | |
| | 623 | 162.0 | 152.3 | 9.5 | 15.1 | |
| | 673 | 121.23 | 111.6 | 8.9 | 18.3 | |
| RAF2* | 298 | 500.0 | 455.8 | 11.5 | 15.6 | 91 |
| | 573 | 274.1 | 236.1 | 6.7 | 10.8 | |
| | 623 | 249.7 | 228.4 | 5.5 | 10.7 | |
| | 673 | 159.1 | 145.6 | 7.6 | 10.3 | |

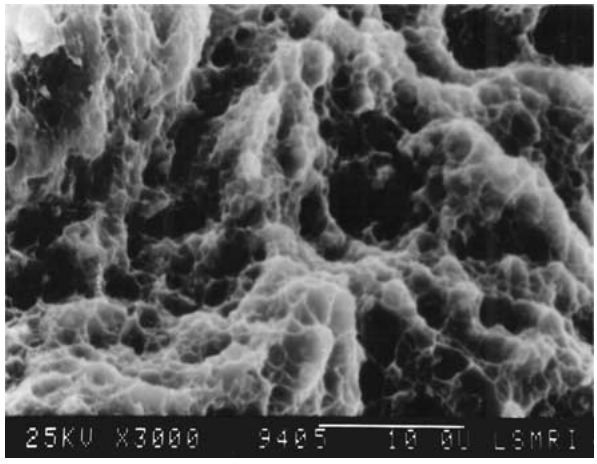


(a)

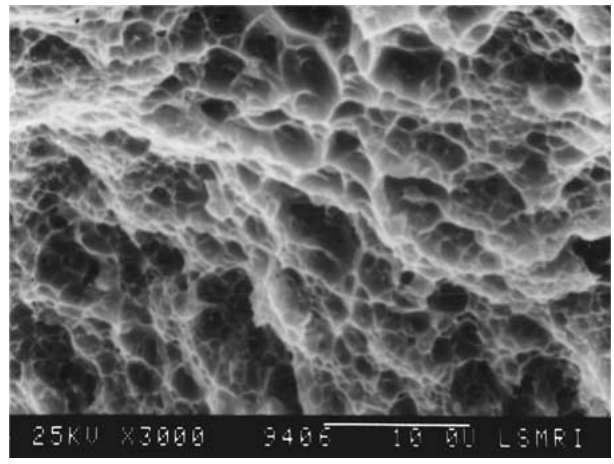


(b)

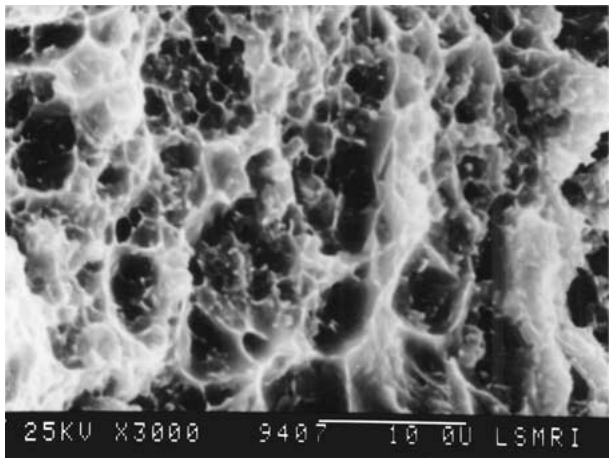


(c)

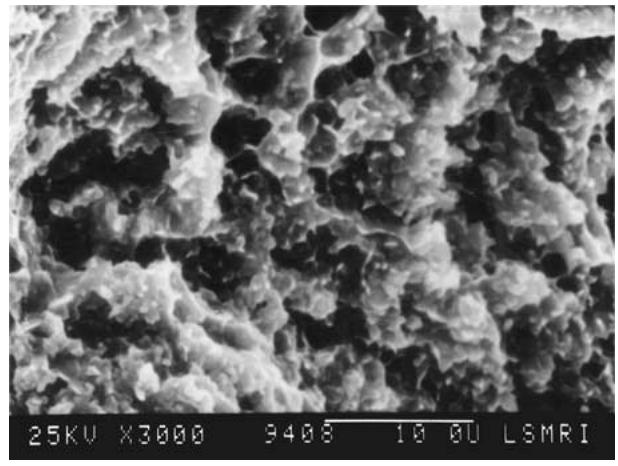


(d)

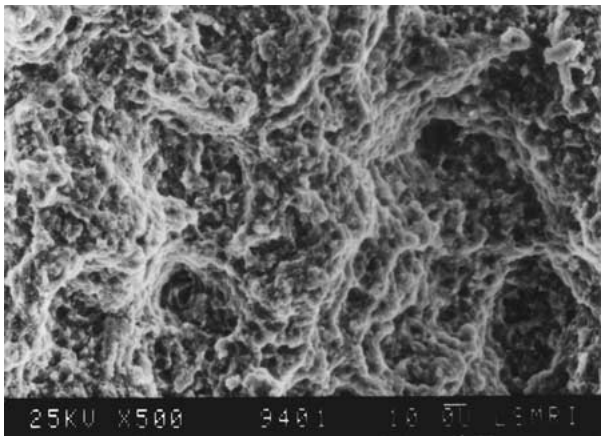


(e)

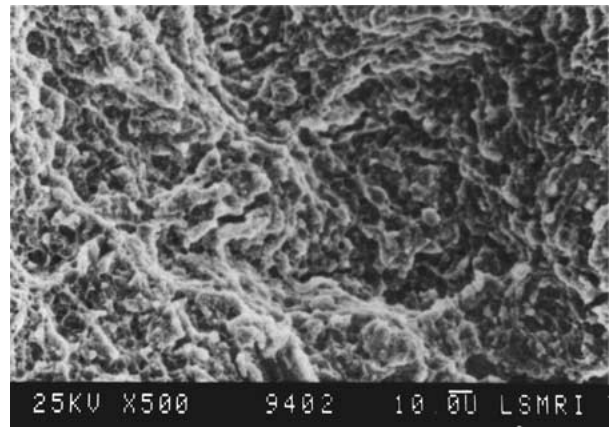


(f)

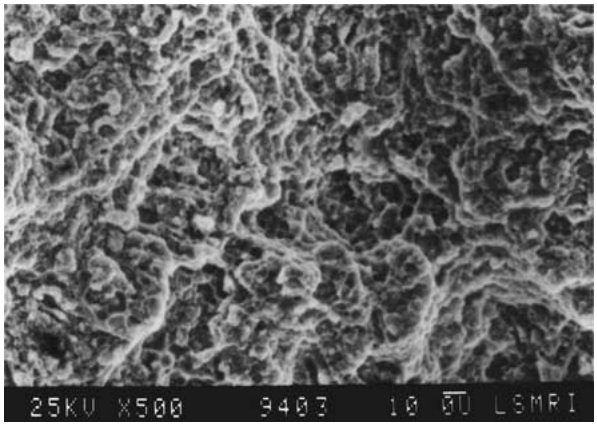


(g)

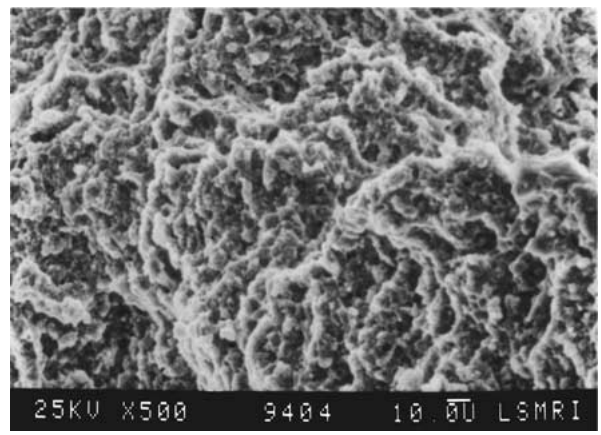


(h)

*Figure 9* SEM micrograph showing the ductile mode of fracture as observed in RS extruded in situ composites of RA20* and RAF2*: RA20* 298 K (a), RA20* 573 K (b), RA20* 625 K (c), RA20* 673 K (d); RAF2* 298 K (e), RAF2* 373 K (f), RAF2* 623 K (g), RAF2* 673 K (h).

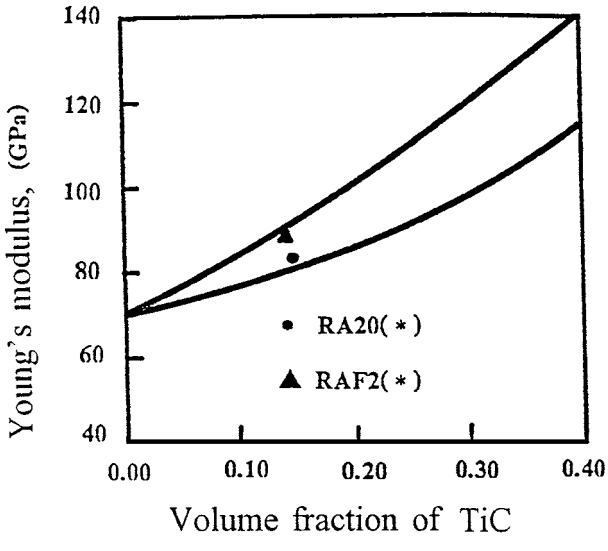


*Figure 10* Variation of Young's modules with volume fraction of TiC, according to Hashin-Shtrikman's model [16]. The data point shows the modules value of the RS in situ Al/TiC composite.

in the range estimated from the equations [15], whereas a mechanically bonded interface will fail to make even the lower bound value. The modulus determined for the RA20* and RAF2* is plotted in Fig. 10 with the lower and upper bound curves as predicted by the H-S equations. The measured values of modules for the RA20* and RAF2* are approximately 81 GPa and 91 GPa, respectively. Therefore, the fact that the modulus of both in situ composites is close to the upper H-S limit and well above the low-limit indicates that the in situ processing leads to a complete chemical interfacial bonding and the attendant load transfer.

## 4.2. Strength

The strengthening mechanism which may operate in particle reinforced MMCs has been considered in several recent publications, and the behavior has also been extensively modeled mathematically [16, 17]. The difficulty with these approaches is that they ignore the influence of particles on the micromechanics of deformation, such as the modifications in microstructures, grain size and dislocation density.

In the micromechanics approach, the principal strengthening mechanisms for the present dispersed particle-hardened RS in situ Al-TiC composites would then include Orowan strengthening, grain-size and substructure strengthening, and solid-solution strengthening. Linear summation of such terms is often used to predict yield strength and the results are

$$y = \sigma_{\text{Orowan}} + \sigma_{\text{grain}} + \sigma_{\text{solute}} \tag{2}$$

other factors, such as lattice friction, have been neglected due to their small magnitudes [18].

### 4.2.1. Orowan strengthening

Orowan strengthening results from interaction between dislocations and the dispersed particles. For strengthening due to the second-phase dispersions, precipitates, and void/cavities, the following expression was used [19]:

$$\sigma_{\text{Orowan}} = \frac{2G\boldsymbol{b}}{2\pi(1-\nu)^{1/2}}\frac{1}{\lambda}\ln(D/\boldsymbol{b}) \tag{3}$$

where $G$ is the shear modulus of the matrix, $\boldsymbol{b}$ is the Burger's vector, $\nu$ is Poisson's ratio, $\lambda$ is the edge-to-edge interparticle spacing, and $D$ is the average particle diameter. A factor of 2 has been included in the numerator to convert the applied stress to resolved shear stress. The interparticle spacing, $\lambda$, can be expressed in terms of the volume fraction ($f_{\text{v}}$) of dispersed (second-phase) particles and the average particle diameter by [19]

$$\lambda = D\left(\frac{\pi}{6V_{\text{f}}} - \frac{2}{3}\right)^{1/2} \tag{4}$$

which can be calculated with the microstructural parameters obtained from the TEM results [8].

### 4.2.2. Grain and substructure strengthening

The flow stress of a material is almost universally observed to increase as the grain size decreases. The grain and substructure strengthening in the present materials appears to be due to the very fine grains via the Hall-Petch type of equation [20]

$$\sigma_{\text{grain}} = \sigma_0 + kd^{-m} \tag{5}$$

where $m = 0.5$, and the other terms are: $\sigma_{\text{grain}}$ = yield strength contribution from grains; $\sigma_0$ = friction stress; $d$ = grain size; and $k$ = material constant. The values for the constants, $\sigma_0 = 15.7$ MPa and $k = 0.07$ were obtained from the literature [21] for pure aluminum.

### 4.2.3. Solid solution strengthening

When a foreign atom dissolves in the matrix it may act as an atomic sized obstacle to the motion of dislocations. If the foreign atom has a different size than the parent atoms, then a misfit strain field will be produced around the foreign atom that may interact with the dislocation strain field. Take the fractional difference in foreign atom diameter and parent atom diameter as $\varepsilon$. Then, for a substitutional solute or an interstitial solute with only a symmetrical strain field, analysis of the strain field-dislocation interaction givens an expression [22]

$$\sigma_{\text{solute}} = G\varepsilon\sqrt{x_{\text{f}}}/4 \tag{6}$$

where $G$ is the elastic shear modulus, $x_{\text{f}}$ is the fractional concentration of the foreign atoms. For the C, Ti and Fe atoms dissolved in the $\alpha$-Al matrix, the fractional difference in these atom diameters and the matrix atom diameter are 0.362, 0.0391 and 0.1333, respectively.

Using the data shown in Table IV, values of $\sigma_{\text{Orowan}}$, $\sigma_{\text{grain}}$ and $\sigma_{\text{solute}}$ calculated from Equation 3, through 6 with relevant parameters are shown in Fig. 11a–c.

As shown in Fig. 11a, the values of $\sigma_{\text{Orowan}}$ largely increased with increasing volume fractions or decreasing diameters of dispersed phase (TiC) particles. In other words, increasing the volume fractions or decreasing diameters of dispersed phase (TiC) particles have equivalent effects on increasing the values of $\sigma_{\text{Orowan}}$.

TABLE IV Parameters used for calculation of mechanical properties [21, 23]

| | Matrix (Al) | TiC |
|---|---|---|
| Young's modules E (GPa) | 72 | 431.0 |
| Poisson's ratio $\lambda$ | 0.34 | 0.19 |
| Bulk modules K (GPa) | 75 | 231.7 |
| Shear modules G (GPa) | 26.9 | 181.1 |
| Thermal coefficient of expansion $C_{ie}$ ($10^{-6}$/K) | 23.6 | 8.6 |
| Friction stress $\sigma_0$ (MPa) | 15.7 | – |
| Burger's vector **b** (nm) | 0.28 | – |

For the present materials, the volume fractions of dispersed particles are about 15 vol.% (RA20*) and 30 vol.% (RAF2*), when the particle diameter $D = 40$–80 nm, the values of $\sigma_{\text{Orowan}}$ are 120–270 MPa and 200–350 MPa, respectively (dotted line in Fig. 11a). Fig. 11b shown various of $\sigma_{\text{grain}}$ vs matrix grain diameter, $d$. When $d = 0.4$–$0.8$ $\mu$m, $\sigma_{\text{grain}} = 90$–120 MPa for the present RS Al-TiC dispersed strengthening composites (dotted line in Fig. 11b). Fig. 11c shows how values of $\sigma_{\text{solute}}$ vary with the fractional concentration of C, Ti and Fe. Comparatively, the interstitial C is most effective, the substitutional solutes Fe takes second place, Ti is relatively poor in increasing the values of $\sigma_{\text{solute}}$. In the present materials, when the values of $x$f for C, Ti, and Fe are 0.3 at%, 0.6 at% and 1.0 at%, the values of $\sigma_{\text{solute}}$ are 130, 20 and 90 MPa, respectively.

According to Equation 2, if $V$f = 15 vol.% (RA20*) and 30 vol% (RAF2*), $D = 40$–80 nm, $d = 0.4$–0.8 $\mu$m, then $\sigma_y = 320$–470 MPa, and 470–770 MPa. The measured values of RA20* and RAF2*, 296 MPa and 416 MPa, close to the lower limit of the calculated values of $\sigma_y$. This implies that the processing parameters could be further improved to bring the materials potential into full play.

The relationship between the flow stress $\sigma_b$ and the yield stress $\sigma_y$ can be given by the Ludwik relation [24],

$$\sigma_b = \sigma_y + k\varepsilon_p^{1/2} \tag{7}$$

where $\varepsilon_p$ is true plastic strain, $k$ is the strain-hardening coefficient, and determined by [24]

$$k = \alpha G[(2\boldsymbol{b}V_f/D) + \boldsymbol{b}/(2L)]^{1/2} \tag{8}$$

where $\alpha$ = constant, typically taken as 0.25. $D$ is the particle diameter in the slip plane, and $L$ is the slip length in the material matrix. The strain-hardening coefficient, $k$, can be evaluated from Equation 8 by using appropriate values of microstructural parameters obtained from the TEM results [8]. Taking $L = 500$ nm, $D = 60$ nm, $V_f = 0.15$, 0.30, then $k = 276$, 373 MPa, $\sigma_b = 337$, 459 MPa, closing to the measured values of $\sigma_b$.

The tensile strength tends to decrease with increasing temperature. According to the experimental data shown in Tables I and II, the variation of the tensile strength with the temperature is given quite well by

$$\sigma_b = 505\text{–}0.55\,T,\ \sigma_{0.2} = 442\text{–}0.47\,T \quad \text{for Al/5Ti-1C(RA20*)} \tag{9}$$

$$\sigma_b = 760\text{–}0.86\,T,\ \sigma_{0.2} = 619\text{–}0.67\,T \quad \text{for Al-Fe-V-Si/5Ti-1C(RFA2*)} \tag{10}$$

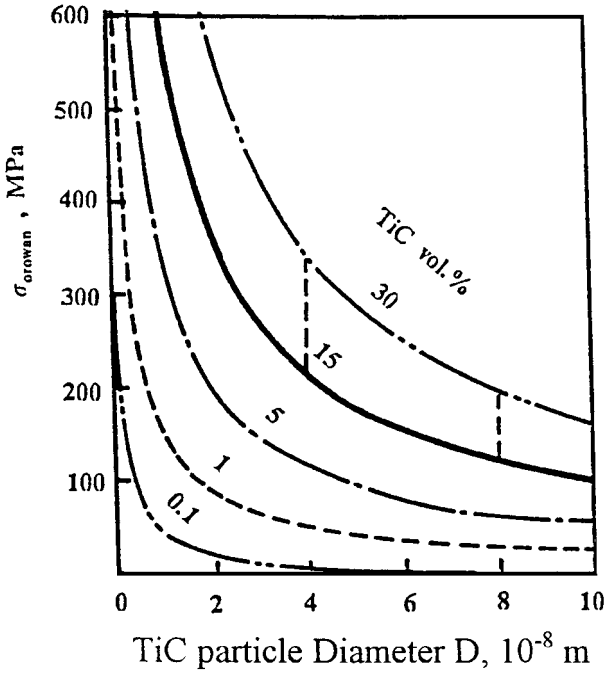


(a)

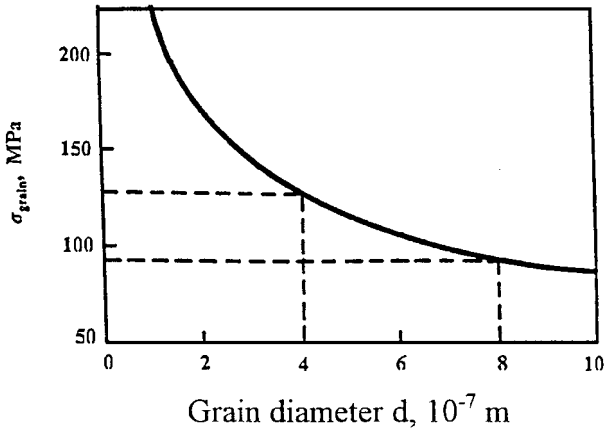


(b)

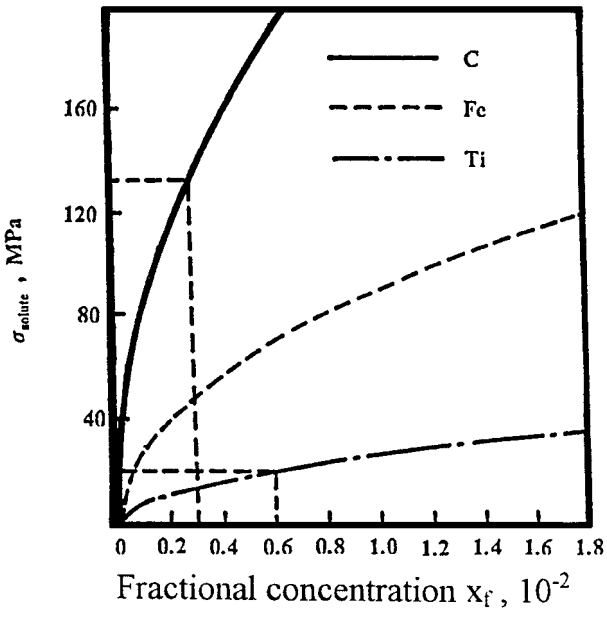


(c)

*Figure 11* Various of $\sigma_{\text{Orowan}}$ (a), $\sigma_{\text{grain}}$ (b) and $\sigma_{\text{solute}}$ (c) calculated from Equation 3 through 6 with relevant parameters. The data points show the relevant measured values of the RS in situ Al/TiC composite.

### 4.3. Elongation

The major limitation in the mechanical properties of composites is the rather limited ductility. However, the composite failure is associated with particle cracking and void formation in the matrix within clusters of particles. Particle cracking by catastrophic propagation f an internal defect is given by the Griffith equation [13]

$$\sigma_f = \left(\frac{2E\gamma}{\pi C}\right)^{1/2} \tag{11}$$

where $\sigma_f$ is the stress on the particle, $\gamma$ the fracture surface energy, $E$ the Young's modules of the particle, and $C$ the internal crack length.

For coarser particles there is a higher probability of their containing a defect of length $C$ sufficient to give particle fracture. It is worth nothing that the particles are being loaded through the particle/matrix interface, so a high degree of particle fracture is indicative of a high interfacial strength, particularly when cracking is occurring in finer particles, $<10\ \mu$m.

A criterion for particle particle-matrix decohesion appropriate for coarse particles has been developed by Argon *et al*. The critical stress for interfacial void nucleation, $\sigma_c$, is given by [13]

$$\sigma_c = \sigma_e + \sigma_m \tag{12}$$

where $\sigma_e$ is the equivalent stress and $\sigma_m$ the mean stress ($\sigma_m = \sigma_{ij}/3$). Void nucleation will therefore be a function of the matrix flow stress, which will be influenced by the volume fraction of particles, heat treatment, etc.

In unreinforced material, voids grow after being nucleated until they are of a sufficient size to coalesce, resulting in final fracture. However, with the high volume fraction of particles in composites, extensive void growth does not occur. The limit load failure model of Thomason predicts the condition for spontaneous ductile fracture at the void nucleation strain as [13]

$$\{0.3[(\pi/4V_f)^{1/2} - 1] + 0.6\}/(1 - V_f) = 1/2 + \sigma_m/2k \tag{13}$$

where $V_f$ is the volume fraction of nucleated voids, $\sigma_m$ the mean stress, and $k$ the matrix shear flow stress.

Considering all these different factors it is clear that the fracture process in particle composites is quite complex, and a quantitative understanding is lacking. It is also apparent that different composites may be dominated by different fracture process, but to maximize ductility for a particular volume fraction, the composite should have:

a. Uniform particle distribution.
b. A fine, uniform particle size distribution.
c. A high interfacial strength.
d. Control of particle shape.
e. A ductile matrix.

Composite fabrication and processing will influence the degree of flexibility available to meet these requirements. It is the reason that RS was used in the present work.

## 5. Conclusion

1. The results presented in this article suggest that the IM and RS processing may be successfully utilized to manufacture high-strength Al-Si/TiC and high-temperature al-Fe/TiC in situ composites.

2. The microstructural characteristics of IM or RS Al-Si/TiC and Al-Fe/TiC can be thought as a combination of the related alloy matrix microstructures and the IM or RS Al/TiC composites.

3. The IM Al/TiC(IA20) and the Al-Si/TiC(IAS0) show superior strength and percentage elongation to the relevant aluminum based composites.

4. The RS Al/TiC(RA20*) and the Al-Fe/TiC(RAF2*) exhibit high Youngís module and substantial improvements in room and elevated temperature tensile properties compared to those of rapidly solidified alloys and conventional composites.

5. The Youngís modules values of RS Al/TiC composites are well within Hashin-Shtrikman limits in keeping with the strong interfacial bonding.

6. In the micromechanics approach, the principal strengthening mechanisms for the present dispersed particle-hardened RS in situ Al-TiC composites include Orowan strengthening, grain-size and substructure strengthening, and solid-solution strengthening.

7. RS was used in the present work to maximize strength and ductility for a particular volume fraction, and influence the degree of flexibility available to meet these requirements: uniform particle distribution; a fine, uniform particle size distribution; a high interfacial strength; control of particle shape; and a ductile matrix.

## References


1. C. P. YOU, M. DOLLOR, A. W. THOMPON and I. M. BEMSTEIN, *Met. Trans.* **22A** (1991) 2445.
2. C. C. PERNG, J. R. HWANG and J. L. DOONG, *Compos. Sci. Tech.* **49** ( 1993) 225.
3. A. K. KURUVILLA, K. S. PRASAD, V. V. BHANUPRASAD and Y. R. MAHAJAN, *Scripta Metall.* **24** (1990) 873.
4. W. KAI, J. M. YANG and W. C. HARRIGAN, *Jr. Scr. Metall. Mater.* **23** (1989) 1277.
5. P. K. ROHATIGI, *Key Eng. Mater.* **104–107** (1995) 293.
6. P. C. MAITY and S. C. PANIGRAHI, *ibid.* **104–107** (1995) 313.
7. A. CHRYSANTHOU, *ibid.* **104–107** (1995) 381.
8. X. C. TONG, *J. Mater. Sci.* **33** (1998) 5365.
9. *Idem*., Ph.D. thesis, Tsinghua University, Beijing, 1995.
10. A. BLOYCE and J. C. SUMMER, in "Metal Matrix Composites," edited by G. Chadwick and L. Froyen (E-MRS, North Holland, 1991) p. 231.
11. R. MITRA, M. E. FINE and J. R. WEERTMAN, *J. Mater. Res.* **8** (1993) 2370.
12. V. V. BHANUPRASAD, M. A. STALEY, P. RAMAKRISHNAN and Y. R. MAHAJAN, *Key Eng. Mater.* **104–107** (1995) 495.
13. D. J. LOYDS, *Inter. Mater. Rev.* **39** (1994) 1.
14. S. K. DAS, P. S. GILMAN and D. RAYBOULD, *Key Eng. Mater.* **38/39** (1989) 367.
15. R. MITRA, M. E. FINE and J. R. WEERTMAN, *J. Mater. Res.* **8** (1993) 2380.
16. T. CHRISTMAN, A. NEEDLEMAN and S. SURESH, *Acta Metall.* **37** (1989) 3029.
17. H. G. F. WILSDORF, in "Dispersion Strengthened Al Alloys," edited by Y. W. Kim and W. M. Griffith (TMS, Warrendale, PA, 1988) p. 3.

18. D. J. BACON, U. F. KOCKS and R. O. SCATTERGOOD, *Phil. Mag.* **28** (1972) 1241.
19. A. BARBACKI and W. FRACKOWIAK, *Z. Metallkd.* **79** (1988) 410.
20. L. C. DZVIS and J. E. ALLISON, *Met. Trans.* **24A** (1993) 2487.
21. M. K. PREMKUMAR, A. LAWLEY and M. J. KOCZAK, *Mater. Sci. Eng.* **174** (1994) 127.
22. JOHN D. VERHOEVEN, "Fundamentals of Physical Metallurgy" (John Wiley & Sons, Inc., 1975) p. 518.
23. R. J. MCELROY and Z. C. SZKOPIAK, *Int. Met. Rev.* **17** (1972) 175.
24. S. MITRA and D. MCNELLEY, *Met. Trans.* **24A** (1993) 2589.

*Received 20 November 1997*
*and accepted 28 September 1999*